Supporting Information

Nickel Embedded Carbon Nanostructures as Noble Metal-Free Catalysts for Hydrogen Evolution Reaction

*Sarvesh Kumar[a], Rajeev Kumar[a], Naveen Goyal[a], Ankit Yadav[a], Swetha B.M[b]. and Balaram Sahoo[a,]**

[a]Materials Research Centre, Indian Institute of Science, Bengaluru -560012, Karnataka, India

[b]Department of Mechanical Engineering, MS Ramaiah Institute of Technology, Bengaluru-560054, Karnataka, India

*Corresponding author's email- bsahoo@iisc.ac.in

Telephone No +91-80-2293 2943

S1. Experimental section

S1.1 Materials and Method

For the synthesis of graphite-coated nickel particles embedded in a porous carbon matrix, Nickel (II) acetylacetonate(Sigma-Aldrich, ≥ 99.0% purity) and melamine (97.5% purity) have been used as precursor, and deionized water as solvent. The details of the synthesis procedure have been discussed below.

S1.2 Synthesis procedure

15 ml of deionized water was taken in a 100 ml capacity beaker. Into this,100 mg of melamine was added, followed by a dispersion of 500 mg of nickel (II) acetylacetonate at 60 °C. It was then homogenized using a magnetic stirrer for 30 minutes. A homogenized solution was kept overnight inside a hot air oven at 70 °C to evaporate water. A dry compound was obtained as a product after the completion of the reaction. The resultant compound was taken inside a quartz tube at one end, and a rubber bladder filled with N_2 gas was fixed at the other end of the quartz tube. This whole setup was inserted into a tube furnace, and the temperature of the furnace was raised to 950 °C at a heating rate of 3 °C/min. The temperature was maintained at 950 °C for 30 min for the pyrolysis reaction to occur. After the reaction was completed, the blackish powder product was washed with DI water and ethanol alternatively several times to remove unreacted compounds. After that, the obtained product was dried overnight at 60 °C in a hot air oven to get the final product as Ni nanoparticles embedded carbonaceous materials. A similar procedure was employed to synthesize more samples by varying the amount of melamine (250 mg and 500 mg). The samples prepared using 100, 250, and 500 mg of melamine are named Ni-NY (where Y= 100, 250, and 500). The synthesis procedure used is depicted in **Scheme** 1.

S1.3 Structural characterization

The structure of the as-synthesized materials was characterized by many different techniques. To determine the phase purity of the samples, the X-ray diffraction (XRD) technique was used. The XRD data were recorded in the range 10-60° with a scan rate of 0.06 deg/sec

using a PANalytical Xpert pro instrument with Cu-K_α radiation (λ= 1.541 Å). For the study of morphology and microstructure, an Ultra-55 Zeiss field-emission scanning electron microscope (SEM) equipped with an EDS detector and an FEI Tecnai T20 super twin Transmission electron microscope (TEM) was used. The Raman analysis was carried out using the LabRam HR instrument with a 532 nm laser to estimate the amount of defects in the samples. For estimation of the composition of the samples, XPS spectra of the samples were recorded using a monochromatic Al-K_α X-ray radiation source, operating at 15 kV and 6 mA, for all data acquisitions. The area under the respective XPS spectrum was integrated. The obtained area was normalized with a sensitivity factor. The atomic percentage was calculated using equationS1, as mentioned below [1].

$$\text{At. \%} = \frac{\frac{A_i}{SF_i}}{\sum_i \frac{A_i}{SF_i}} \times 100 \qquad \text{(S1)}$$

Where, i= Ni/C/N; A_i: area under the curve of respective elements, SF_C = 0.25, SF_N = 0.42, and SF_{Ni} = 4.5

S1.4 Details of electrochemical measurements

The electrochemical measurements were carried out using the three-electrode system in N_2-saturated aq. 1M KOH solution with Hg/HgO as the reference electrode, Pt was used as the counter electrode, and the Glassy carbon electrode (GCE) was used as the working electrode. For clarity regarding Pt dissolution, studies were also carried out with graphite as a counter electrode. An ink solution was prepared by dispersing 1 mg of Ni-NY (Y= 100, 250, and 500) catalyst in 1ml of ethanol and sonicated for about 20 min along with 10 µl of Nafion (Nafion solution: 5 wt.% in lower aliphatic alcohols and 15-20% water). The electrode was then dried for 1 hour at 60 °C. Then, the electrochemical measurements were performed in an N_2-saturated alkali medium, as mentioned below. The reference electrode (Hg/HgO) was calibrated against a reversible hydrogen electrode (RHE), as shown in **Fig**. S8. For the calibration, we have used the following equation-S2.

$$E(RHE) = E(Hg/HgO) + 0.969 \qquad \text{(S2)}$$

The impedance spectra were recorded in the frequency range of 10 mHz -1 MHz in different applied potential ranges of HER.

S2. Results

S2.1 Characterization

S2.1.1 XRD analysis

The asymmetric (002) Bragg peak (for graphitic carbon), present at 2θ of ~26.5°can be contributed by the amorphous and graphitic carbon present in the samples. This peak is fitted with two sub-peaks; the broad peak seen on the left shoulder indicates the highly defective amorphous type of carbon (a-C), and the sharper peak on the right-hand side indicates the graphitic type of defective carbon (g-C). These peaks are least-squares fitted accordingly, as shown in **Fig**. S1 (a), (c), and (e). It can be expected that as the amount of the nitrogen precursor increases, a higher amount of nitrogen gets doped into the graphitic structure or the carbon sheets. Simultaneously, as it is observed that the amorphous carbon content gradually becomes less in the samples, the relative amount of a-C to g-C, i.e., (a-C/g-C) content decreases. The amount of a-C content for the Ni-N100, Ni-N250, and Ni-N500 samples is ~38.5%, ~24.6 %, and ~ 22.5%, respectively, as given in **Table-**S1. Clearly, the degree of graphitization is improved with increased melamine amount. This trend follows the overall I_G/I_D ratios (Raman data, **Fig.** 1(b)), it should be noted that the especially amorphous carbon content (I_{D3}/I_G) also follows this trend. These aspects will be discussed in detail later. In general, the broadening of the carbon peaks is due to the intrinsic defects and the doped foreign atoms (nitrogen) in the samples, which appends extra intrinsic defects in the samples.

Table S1. The 2θ peak position and their composition analysis for amorphous and graphitic carbon on samples Ni-N100, Ni-N250, and Ni-N500, respectively.

Samples	Peak position (°)		Composition (%)	
	Amorphous C	Graphitic C	Amorphous C	Graphitic C
Ni-N100	25.43	26.58	38.5	61.5
Ni-N250	25.41	26.57	24.6	75.4
Ni-N500	25.40	26.56	22.5	77.5

S2.1.2 Raman analysis

The Raman spectra confirm the presence of amorphous carbon through the peak (D3) at 1462 cm^{-1}, along with other defect peaks coded as D1, D2, and D4, where D1 (1350 cm^{-1}) represents the structural defects in sp^2 bonded carbon, D2 (1605 cm^{-1}) represents the defects associated with a carbon atom in edges of graphitic crystallites, and D4 (1195 cm^{-1}) peak arises due to the stretching vibration in conjugated systems. The spectra are matched with these sub-peaks, as illustrated in **Fig**. S1. (b), (d), and (f). For the Raman spectra, all the peaks fit with various sub-peaks, as mentioned.

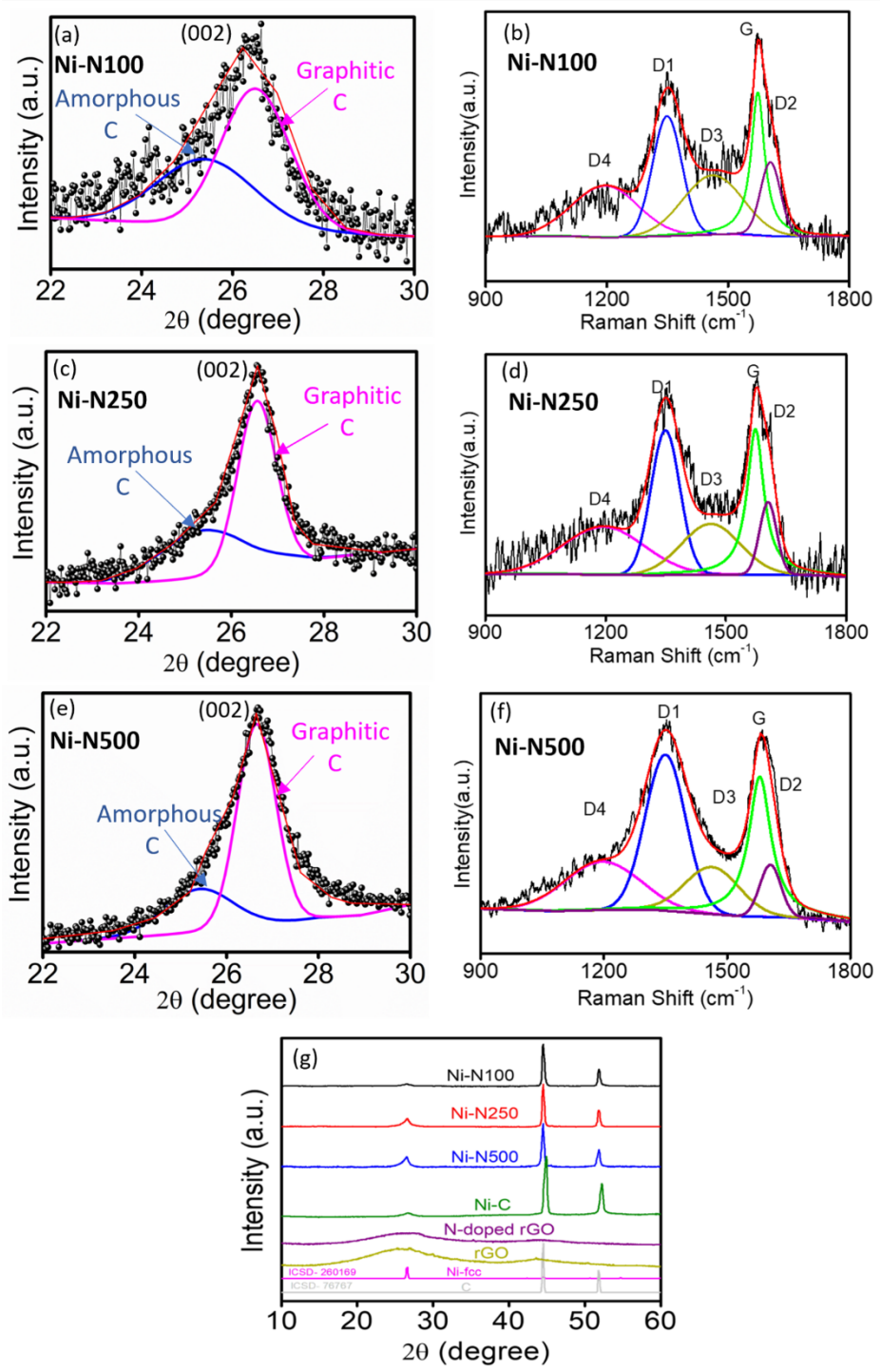

Fig. S1(a), (c), and (e) show the XRD peak fitting of C (002) for Ni-N100, Ni-N250, and Ni-N500, respectively. (b), (d), and (f) show the Raman peak fitting into various constituents for Ni-N100, Ni-N250, and Ni-N500, respectively, and (g) shows the XRD pattern of Ni-NY samples along with our Ni-C, N-doped rGO, and rGO samples.

Table S2. Intensity ratio of graphitic to defective peak on samples Ni-NY (Y = 100, 250, and 500).

Samples	I_G/I_D	I_{D1}/I_G	I_{D2}/I_G	I_{D3}/I_G
Ni-N100	0.34	1.05	0.51	0.98
Ni-N250	0.29	1.52	0.34	0.81
Ni-N500	0.24	1.93	0.23	0.65

S2.1.3 SEM analysis

All samples have similar morphologies, regardless of the amount of N-precursor used during synthesis. The nanoscale white regions observed in the micrographs correspond to the Ni nanoparticles because more secondary electrons are emitted from these particles, which makes the Ni nanoparticles appear white (because the Ni (metal) atoms emit more secondary electrons than the C-atoms). Carbon atoms generate fewer secondary electrons than nickel; hence, they seem slightly grey in hue. Comparing the SEM micrographs of all three samples indicates that the Ni-nanoparticles in the Ni-N100 sample are more localized than those of the Ni-N250 and Ni-N500 samples. Ni-N500 sample has better dispersed Ni-nanoparticles.

S2.1.3.1 SEM-EDX

From the SEM-EDX micrograph, the uniform elemental distribution of C, N, and Ni has been observed in the sample. It is observed that nickel concentration decreases with an increase in the amount of nitrogen (melamine) concentration from Ni-N100 to Ni-N500. During the synthesis, nickel (II) acetylacetonate was used in 750 mg (i.e., 2.65 mmol of nickel). The 12 carbon atoms present in this structure contribute 31.8 mmol carbon concentration source. Because the metal precursor is employed in the same amount for all syntheses and only changes in nitrogen concentration, three carbon atoms from melamine also contribute as a carbon source. The three carbon atoms of melamine contribute 2.37, 5.88, and 11.88 mmol of carbon for 100, 250, and 500 mg of melamine, respectively (**Table** S3). Now, the total carbon content during the synthesis of the compounds is 34.17, 37.68, and 43.68 mmol for 100, 250, and 500 mg of melamine, respectively, which increases the total volume of crystallites. However, the same amount of nickel is distributed throughout the increased crystallite volume. Therefore, we observed the highly densely packed nickel in the low carbon content of the fixed volume. With

increased crystallite volume, the same amount of nickel exhibits poor density in a fixed volume (**Fig**. S2).

Table S3. The amount of C from different sources of the samples Ni-NY (Y = 100, 250, and 500).

Precursor	**Ni-N100**	**Ni-N250**	**Ni-N500**
Nickel(II)acetylacetonate	C=31.8 mmol Ni=2.65 mmol	C=31.8 mmol Ni=2.65 mmol	C=31.8 mmol Ni=2.65 mmol
Melamine	C=2.37 mmol	C=5.88 mmol	C=11.88 mmol
Total C content	34.17 mmol	37.68 mmol	43.68 mmol

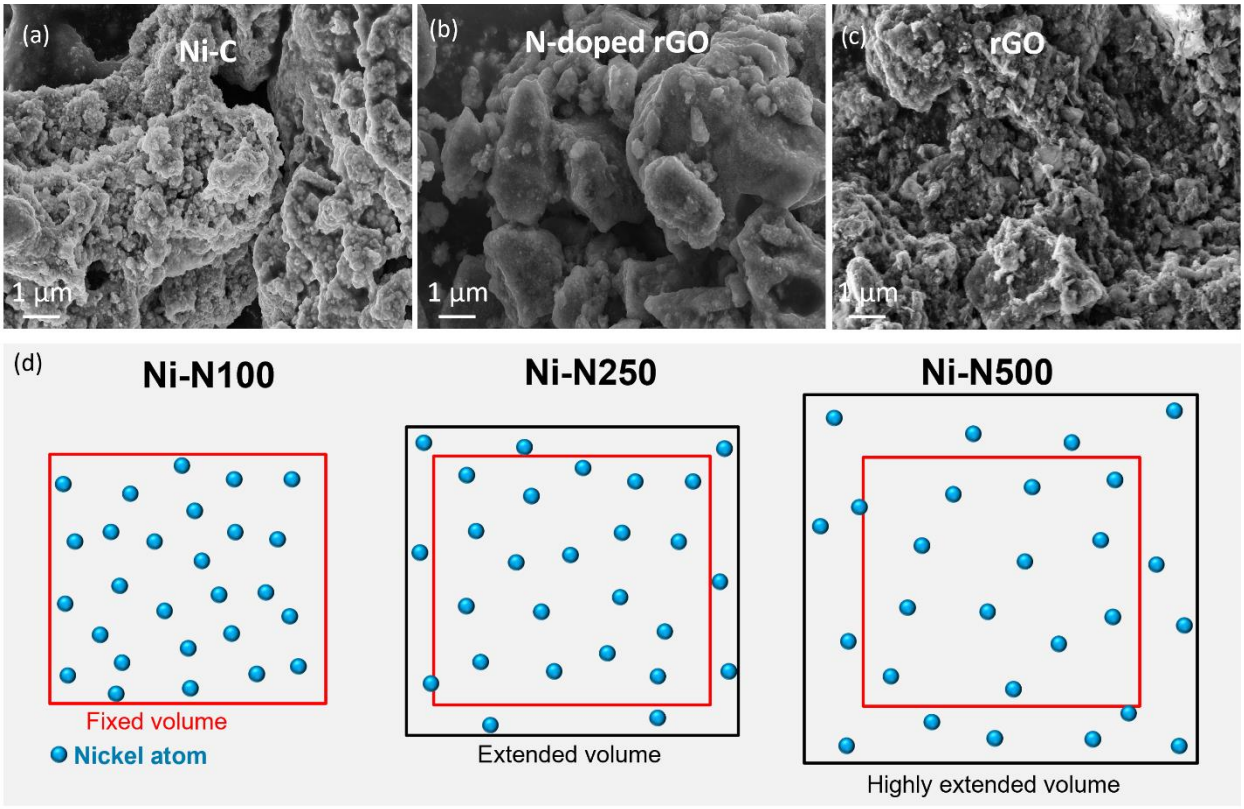

Fig. S2 The SEM micrographs for Ni-C, N-doped rGO, and rGO samples are shown in (a), (b), and (c), respectively, and (d) The schematic of nickel element distribution in EDX imaging for Ni-N100, Ni-N250, and Ni-N500.

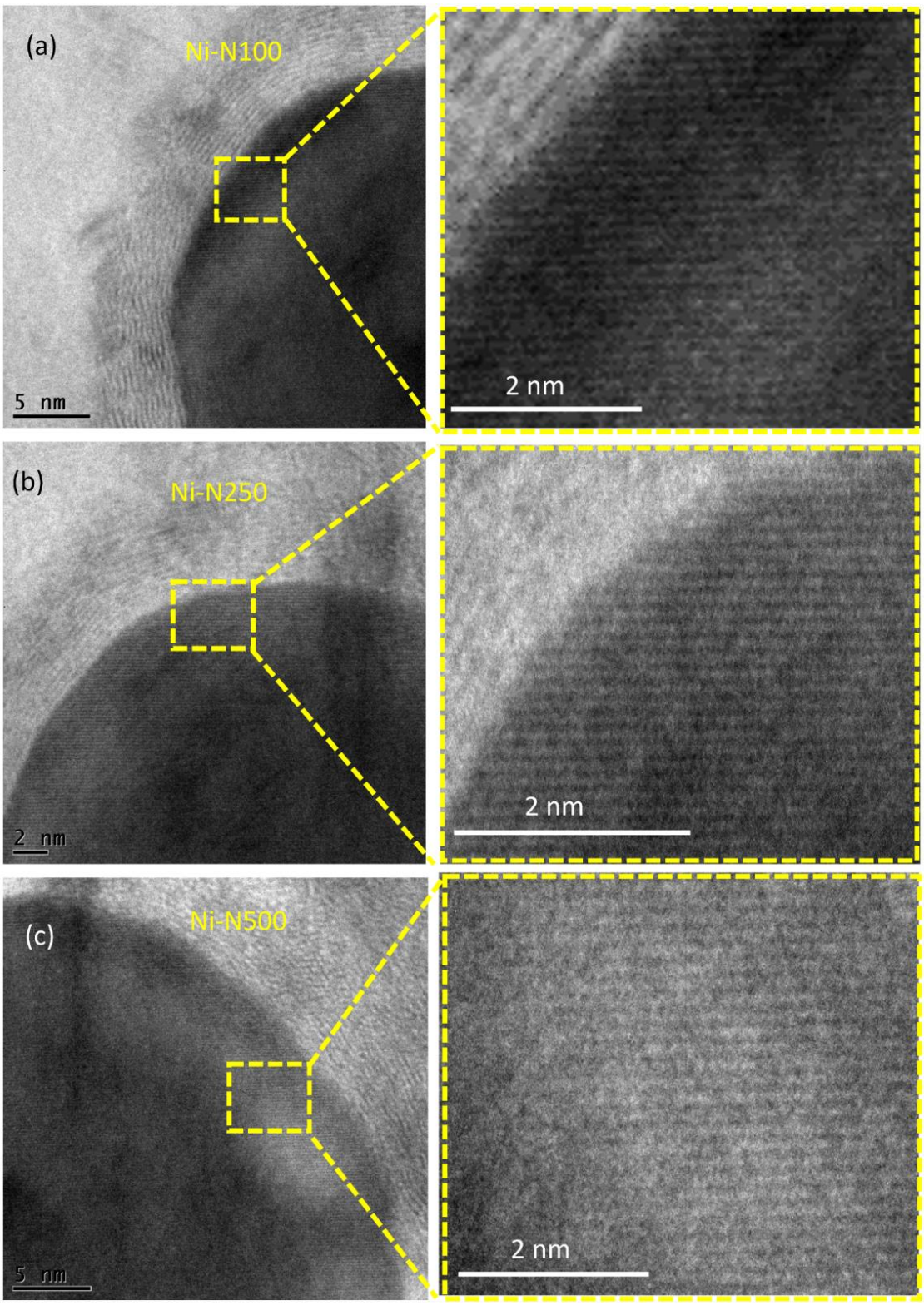

Fig. S3 (a), (b), and (c) are zoomed views of the TEM image of the Ni (111) plane for the Ni-N100, Ni-N250, and Ni-N500 samples, respectively.

S2.1.4 BET analysis

The N_2 adsorption/desorption curves obtained for all the samples exhibit the type IV isotherm and hysteresis behavior that suggest the occurrence of capillary condensation. From the adsorption/desorption curve, it seems that initially, all the sites of heterostructures are vacant. Still, on applying slight relative pressure, there is a sudden increase in the adsorption volume. This occurs because the adhesion energy between the adsorbate molecule and the sample heterostructure is stronger than the cohesive energy between the N-atoms. This process occurs until the heterostructure surface is fully covered with adsorbed nitrogen. This reaches towards the saturation forming a monolayer; hence, an almost flat curve was observed for this condition. Once after the formation of the monolayer, further adsorption occurs on the monolayer surface due to cohesion. In **Fig.** 3(c), a sharp increase in adsorption volume is observed after the relative pressure (P/P_o) value exceeds ~ 0.5. This can originate due to multilayer formation on the flat surface or condensation of a nitrogen molecule in the capillaries (capillary condensation). In the case of desorption, the outermost adsorbed molecule starts to come out and quickly leaves the surface by lowering the relative pressure, and for this, it follows a different path. After reaching the monolayer by lowering the relative pressure, the adhesion energy between the heterostructure and nitrogen molecule becomes the same as in the adsorption process; therefore, adsorption and desorption curves overlap. Versatile morphology may facilitate the penetration of adsorbate gas molecules into the inner layer of materials and considerably improve sensing performance.

An observation of the sample reveals a flip in pore volume as the pore diameter increases (**Fig**. 3(d)). For example, the values of pore volumes for 4 nm pore diameter are 0.11, 0.15, and 0.17 $cm^3\ g^{-1}$ for the samples Ni-N100, Ni-N250, and Ni-N500, respectively. However, for the pore diameter of 9 nm, the Ni-N250 sample exhibits a greater pore volume than the Ni-N500 sample. Please note here that there is a change in the order of the samples with increasing pore size. Similarly, for pores having 11 nm diameter, the pore volumes are 0.026, 0.041, and 0.047 $cm^3\ g^{-1}$ for Ni-N100, Ni-N500, and Ni-N250, respectively.

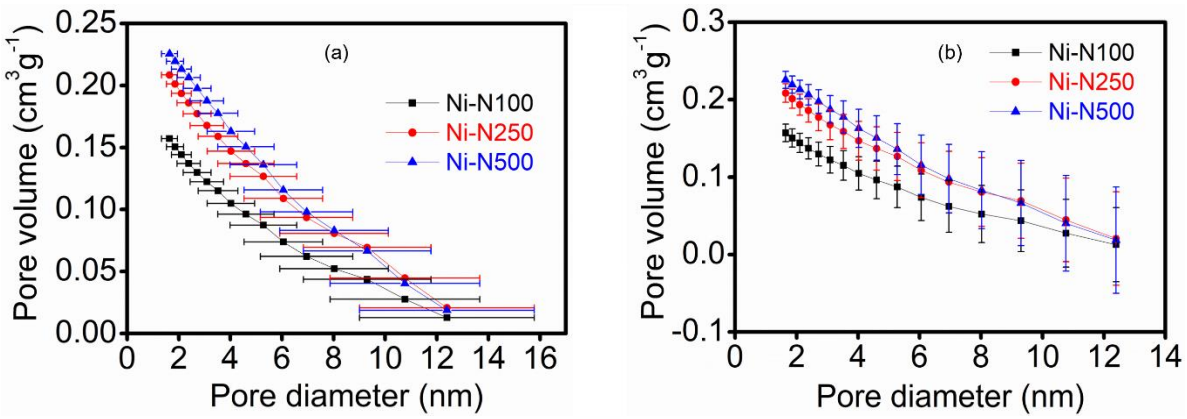

Fig. S4 Standard deviation in pore size (a) and pore volume (b) on Ni-NY (Y = 100, 250, and 500) samples.

The standard deviation in pore volume and pore diameter is calculated using the following formula.

$$S_x = \sqrt{\frac{\sum_{i=1}^{n}(x-\bar{x})^2}{n-1}}$$

Where S_x is the standard deviation, n is the number of data points, x is each value of the data point, and $\bar{x}$ is the mean of x (= Sum/n).

S2.1.5 XPS analysis

The linewidth of the XPS spectra of C1s (**Fig**. S6(a), (d), and (g)) corresponding to various carbon functionalities provide the signature that successfully incorporation of N-atoms into the carbon matrix, which modifies the electronic structure of the samples and facilitates in improving their electrocatalytic activity. The presence of a nitrogen atom within the carbon framework causes the sample to become more reactive (via creating defects) and amend its electronic delocalization, leading to chemical reactions. This aspect of samples can be understood as follows. In a pristine graphitic carbon framework, carbon 2p (π) electrons are strongly overlapped. They give rise to two parallel planes of highly delocalized π electrons, both above and below the σ-bonded C-layer of the graphenic sheets [2]. However, the interruption of the 2p (π) electron continuity can be addressed by considering the existence of a nitrogen atom within the carbon framework, which results from the disparity in electronegativity between carbon and nitrogen (2.55 and 3.05, respectively) and the sample becomes more reactive than pristine carbon sheets. Furthermore, the variation in nitrogen concentration among Ni-NY samples makes a difference in their electronic delocalization and changes the electronic environment. Hence, by altering the electronic delocalization in the samples, it starts participating in chemical reactions. The samples having such features can have various chemical interactions. This aspect can be clearly observed in the XPS spectra through the FWHM of the prominent C 1s peak (284.6 eV). The high-resolution XPS (HRXPS) spectra of C 1s (left panel), N 1s (middle panel), and Ni 2p (right panel) are shown in **Fig**. S6. The C 1s HRXPS spectra are deconvoluted into different types of carbon peaks, suggesting the presence of various carbon functionalities in the sample. The first intense sub-peak centered at 284.5 eV refers to the presence of sp^2 carbon, in addition to various other functionalities such as sp^3, Csp^3-N/Csp^3-O, Csp^2=N/Csp^2=O, and C-O originating the peaks centered at 285.5, 286.5, 287.5, and 289.5 eV, respectively [3,4].

A visual picture of nitrogen moieties such as pyrrolic, pyridinic, and quaternary nitrogen with electron density at their neighboring carbon is depicted in **Fig**. S5. The deconvoluted N1s spectrum fitted into six different peaks at 397.8, 398.5, 398.9, 399.7, 400.7, and 401.9 eV, which are assigned as pyridinic, Ni-N_xC, amine (NH_2), pyrrolic, quaternary nitrogen, and oxidized nitrogen, respectively [5–7].

The XPS scan was performed in the range of 846 eV to 882 eV to knock out the electron from Ni 2p core shells. The deconvoluted XPS spectrum of Ni 2p, **Fig.** S6 ((c), (f), and (i)), Ni $2p_{3/2}$ emission line has fitted the peak which centered around 852.2, 854.5, and 856.2 eV assigned as nickel metal Ni (0), Ni $2p_{3/2}$ (main), and Ni $2p_{3/2}$ (surface + non-local) peaks in spectra. The Ni $2p_{3/2}$ satellite peak was fitted at 860.5 eV and 864.9 eV. Furthermore, Ni $2p_{1/2}$ (main) and Ni $2p_{1/2}$ (surface + non-local) were served at 870.5 and 874.2 eV, respectively, while the Ni $2p_{1/2}$ satellite peak was fitted at 878.2 and 881.2 eV [3,8]. The dominating spectral contribution of the NiO major phase at 854.5 eV is related to the Ni $2p_{3/2}$, whereas the peak at 856.2 eV was impacted by surface effects and non-local contributions (**Table** S4). Although the earlier reports [9] used the single Gaussian peak for Ni^{2+} (NiO) and the satellite peak, which does not provide deeper meaning to the analysis. Hence, we fitted this peak using two Gaussian peaks assigned at (NiO) and the satellite peak.

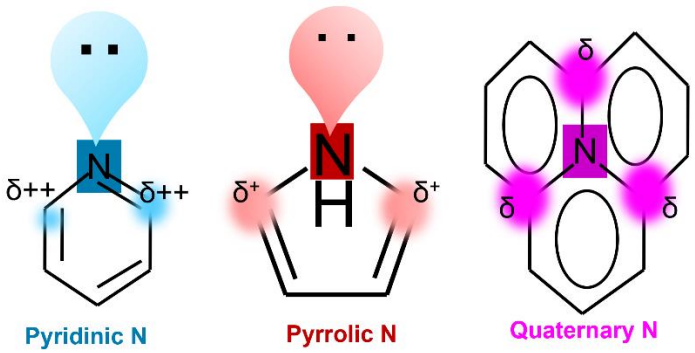

Fig. S5 The different moieties with different neighboring electron densities of carbon atoms.

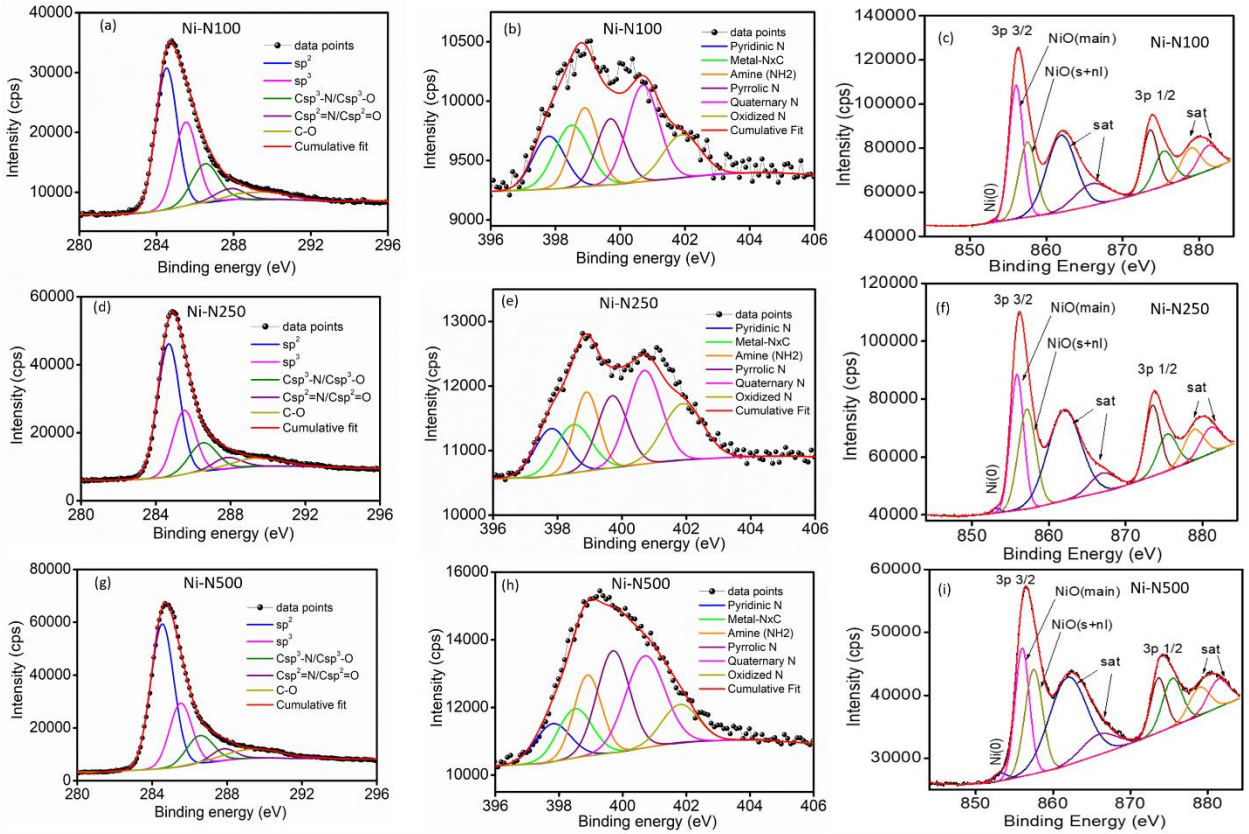

Fig. S6(a), (b), and (c) HRXPS of C1s, N1s, and Ni 2p of Ni-N100 sample, respectively. (d), (e), and (f) HRXPS of C1s, N1s, and Ni 2p of Ni-N250 sample, respectively. (g), (h) and (i) are HRXPS of C1s, N1s, and Ni 2p of Ni-N500 sample, respectively.

Table S4. The table for elements (C 1s, N 1s, and Ni 2p) obtained from XPS, their types, peak positions, and FWHM of respective peaks for our sample Ni-NY (Y=100, 250, and 500).

Element	**Peak**	**Peak position (eV)**	**N-N100** **FWHM (eV)**	**Ni-N250** **FWHM (eV)**	**Ni-N500** **FWHM (eV)**
C 1s	sp^2	284.6	1.32	1.40	1.46
	sp^3	285.5	1.38	1.41	1.42
	Csp^3-N/Csp^3-O	286.4	1.63	1.73	1.68
	Csp^2=N/Csp^2=O	287.5	1.87	1.76	1.50
	C-O	289.5	3.19	3.18	3.55
N 1s	Pyridinic	397.8	1.16	1.20	1.30
	Ni-N_xC	398.5	1.26	1.29	1.26
	Amine (NH_2)	398.9	0.96	0.90	1.02
	Pyrrolic	399.7	1.01	1.09	1.20
	Quaternary	400.7	1.16	1.23	1.45
	Oxidized	401.9	1.36	1.47	1.35
Ni 2p	Ni (0)	852.6	1.18	1.40	2.18
	Ni $2p_{3/2}$ (main)	854.5	3.78	2.05	2.19
	Ni $2p_{3/2}$ (surface + non-local)	856.2	3.75	2.69	2.69
	Satellite, $2p_{3/2}$	860.5	5.60	5.08	5.69
		864.9	3.06	3.94	5.20
	Ni $2p_{1/2}$ (main)	870.5	5.80	2.33	2.34
	Ni $2p_{1/2}$ (surface + non-local)	874.2	4.38	2.97	2.94
	Satellite, $2p_{1/2}$	878.2	3.54	3.05	3.08
		881.2	3.39	3.10	3.14

Table S5. Atomic percentage of nitrogen of different nitrogen functionality (from XPS) for sample Ni-NY (Y=100, 250, and 500).

Samples	**Nitrogen (%)**						**Overall Nitrogen %**
	Pyridinic (N)	**Metal-N_xC**	**Amine (N)**	**Pyrrolic (N)**	**Quaternary (N)**	**Oxidized (N)**	
Ni-N100	0.31	0.40	0.38	0.34	0.57	0.30	2.3
Ni-N250	0.54	0.59	0.68	0.76	1.11	0.82	4.5
Ni-N500	0.82	0.98	1.24	1.76	1.90	0.52	7.2

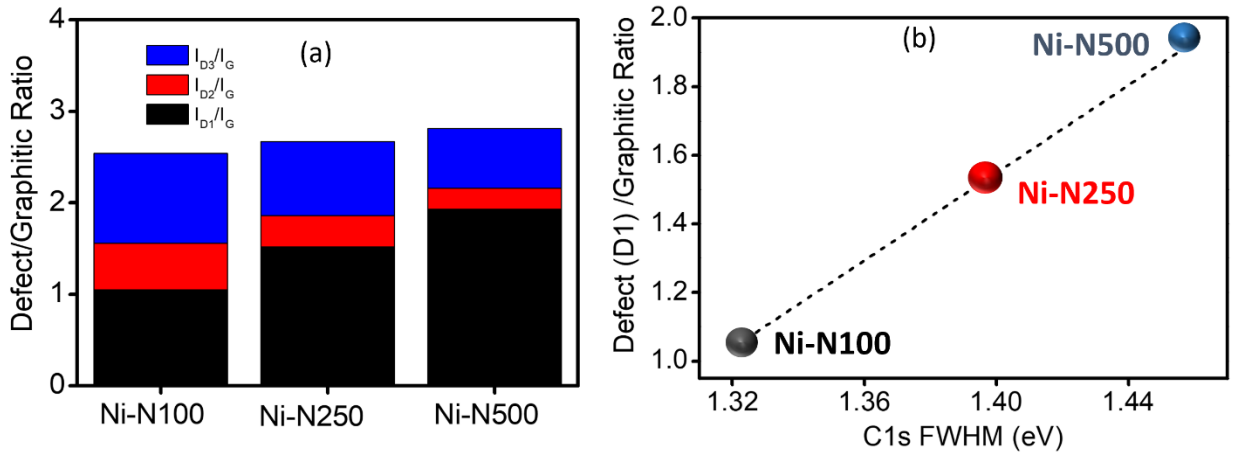

Fig. S7 (a) Defect/graphitic ratio for various defects present in the material, and (b) linear correlation between Defect (D1)/graphitic ratio to C1s FWHM for samples Ni-N100, Ni-N100, and Ni-N500, respectively.

S2.1.6 UV-Vis DRS

For the estimation of the optical band gap, the Kubelka-Munk method was employed using diffused reflectance *F*(R) spectroscopy, where-

$$F(R) = (1-R)^2/2R = k/s \qquad \text{(S3)}$$

where R is measured reflectance, '*k*' is the molar absorption coefficient, and '*s*' is the scattering coefficient.

The energy can be estimated using equation- $E = hc/\lambda$, where *h* indicates Planck constant ($h = 6.63 \times 10^{-34}$ J.s), *c* indicates speed of light ($c = 3 \times 10^8$ m/s), and λ indicates the wavelength of light.

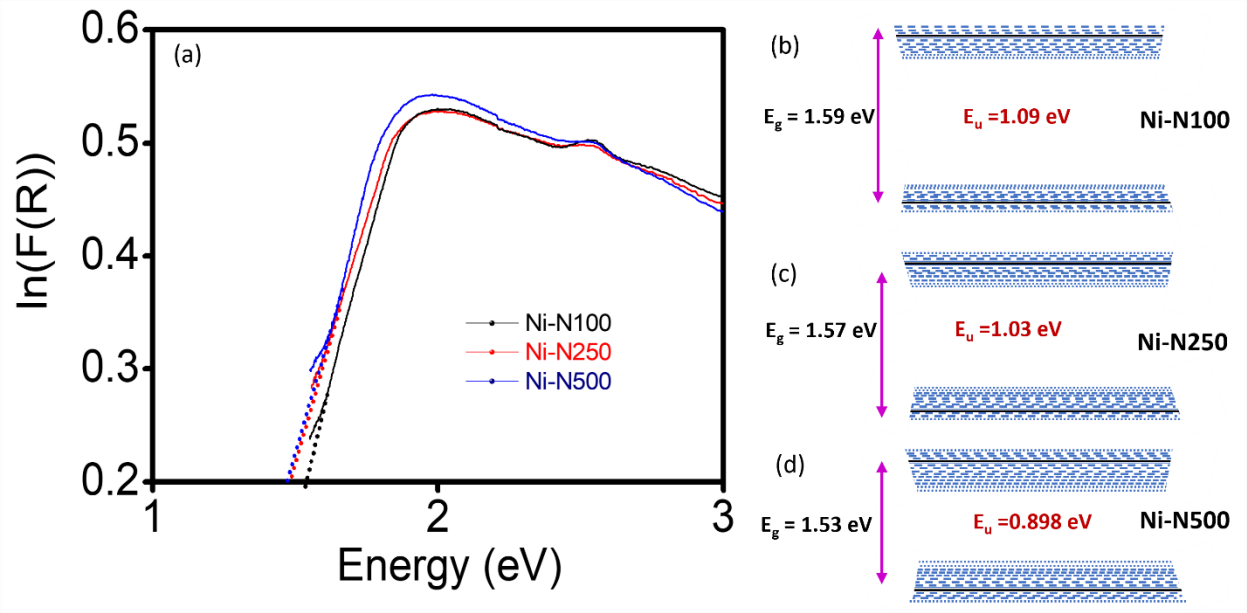

Fig. S8 (a) Plot of ln(F(R)) vs. energy (Urbach energy plot). (b), (c) and (d) show the schematic of the energy level diagram for Ni-N100, Ni-N250, and Ni-N500, respectively. The broken lines represent the defect energy levels forming within a direct bandgap.

S2.2 Electrochemical characterization

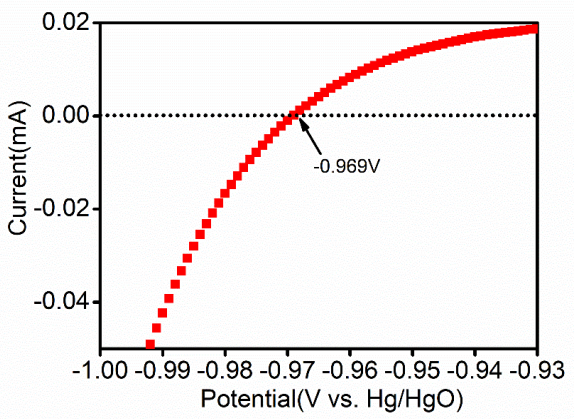

Fig. S9 Hg/HgO electrode calibration against reversible hydrogen electrode (RHE) in aq. 1M KOH solution.

S2.2.1 Mass loading optimization

Catalyst amounts ranging from 0.28, 0.42, 0.56, 0.70, and 0.84 mg/cm^2 were drop-cast on the GC electrode to optimize the catalyst loading. **Fig**. 4(a) illustrates the linear sweep voltammetry (LSV) polarization curves for Ni-N500 at various mass loadings. When the polarization curves for different mass loadings are compared, an increase in catalyst loading results in a considerable increase in the hydrogen evolution reaction (HER) current density, reaching its highest value at 0.56 mg/cm^2. The needed overpotential increased with higher or lower loadings. **Fig**. 4(b) presents a correlation plot showing the relationship between overpotential (@100 mA/cm^2) and electrode mass loading. The surface lacks sufficient coverage below a mass loading of 0.56 mg/cm^2, leading to fewer available active sites. Conversely, when the catalyst loading exceeds 0.56 mg/cm^2, the diffusion path length of electrons within the material hinders electronic communication between the surface of the catalyst (where the HER is occurring) and the current collector (GC electrode) [10]. When the catalyst loading reaches its optimal value of 0.56 mg/cm², it entirely covers the electrode surface, ensuring the highest coverage, maximizing the amount of active centers, and resulting in a higher current at a small overpotential. The observation of the highest current density and lowest overpotential occurred at a catalyst loading of 0.56 mg/cm²; the GC electrode with this mass loading was selected for further electrochemical studies.

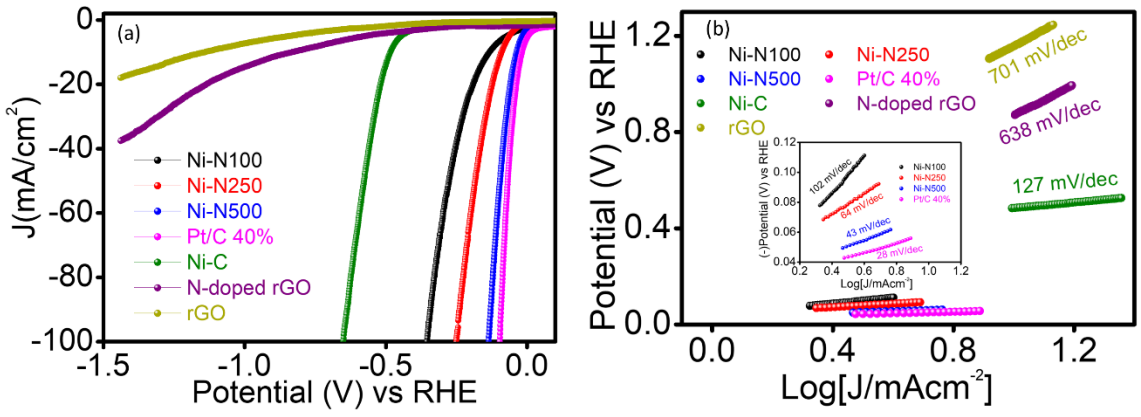

Fig. S10 (a) HER polarization curves, as well as (b) Tafel plots for Ni-NY samples along with Ni-C, N-doped rGO, and rGO samples.

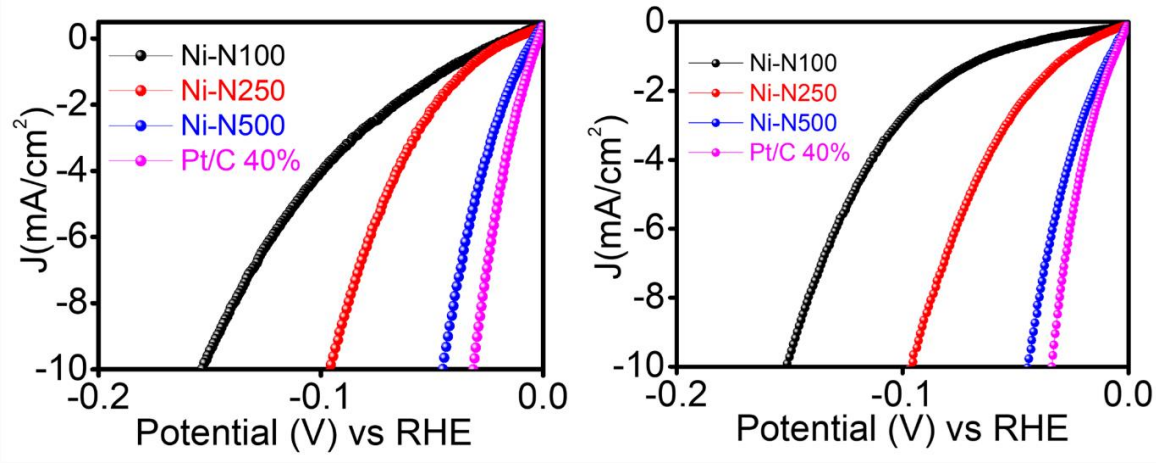

Fig. S11 LSV polarization curves on Ni-NY samples and Pt/C using a counter electrode as Pt wire (left side) and graphite rod (right side).

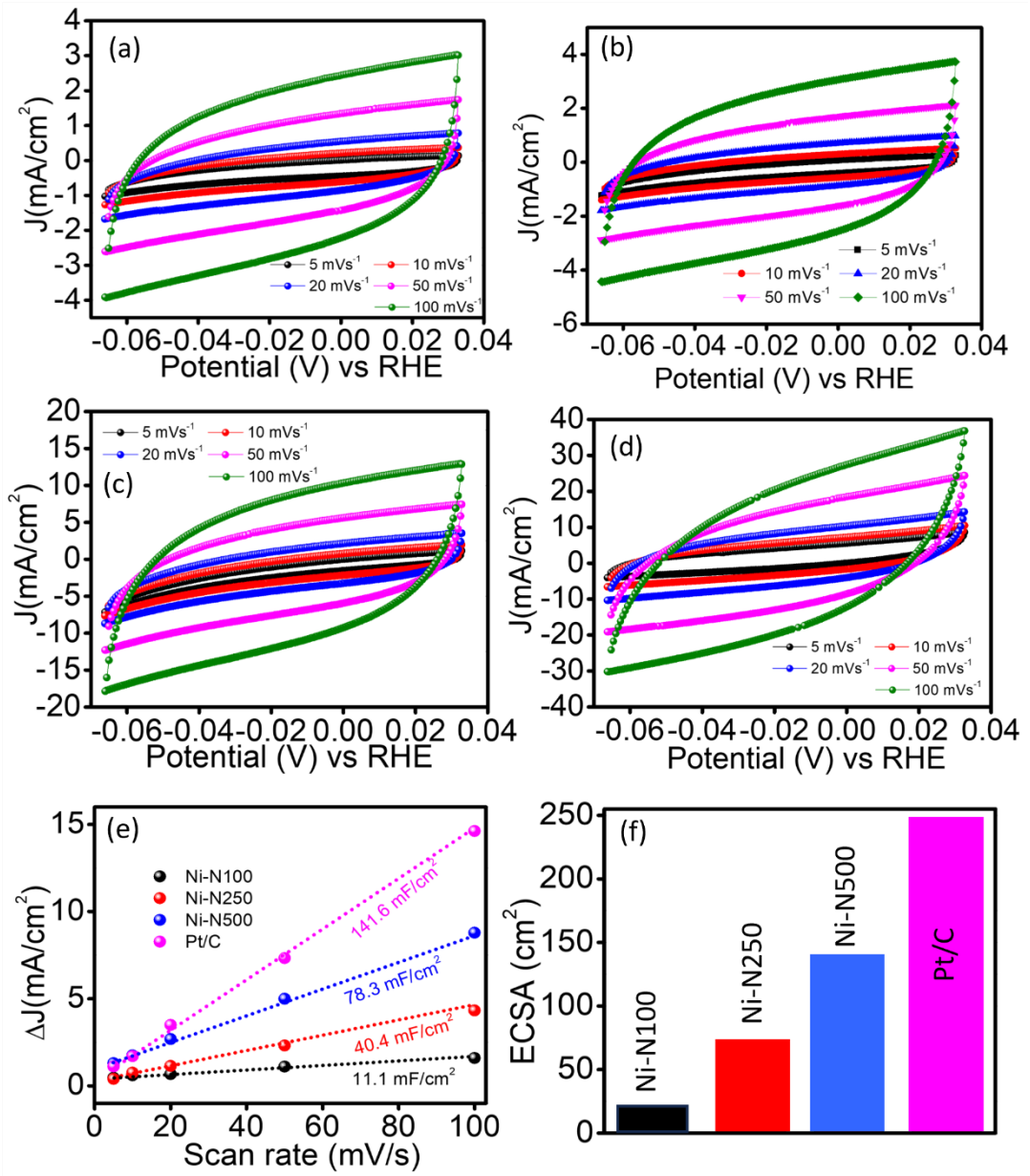

Fig. S12 (a), (b), (c), and (d) CV at different scan rates (5, 10, 20, 50, and 100 mV/s) for Ni-N100, Ni-N100, Ni-N100, and Pt/C samples, respectively. (e) C_{dl} estimation, and (f) estimated electrochemical active surface area for Ni-NY and Pt/C samples.

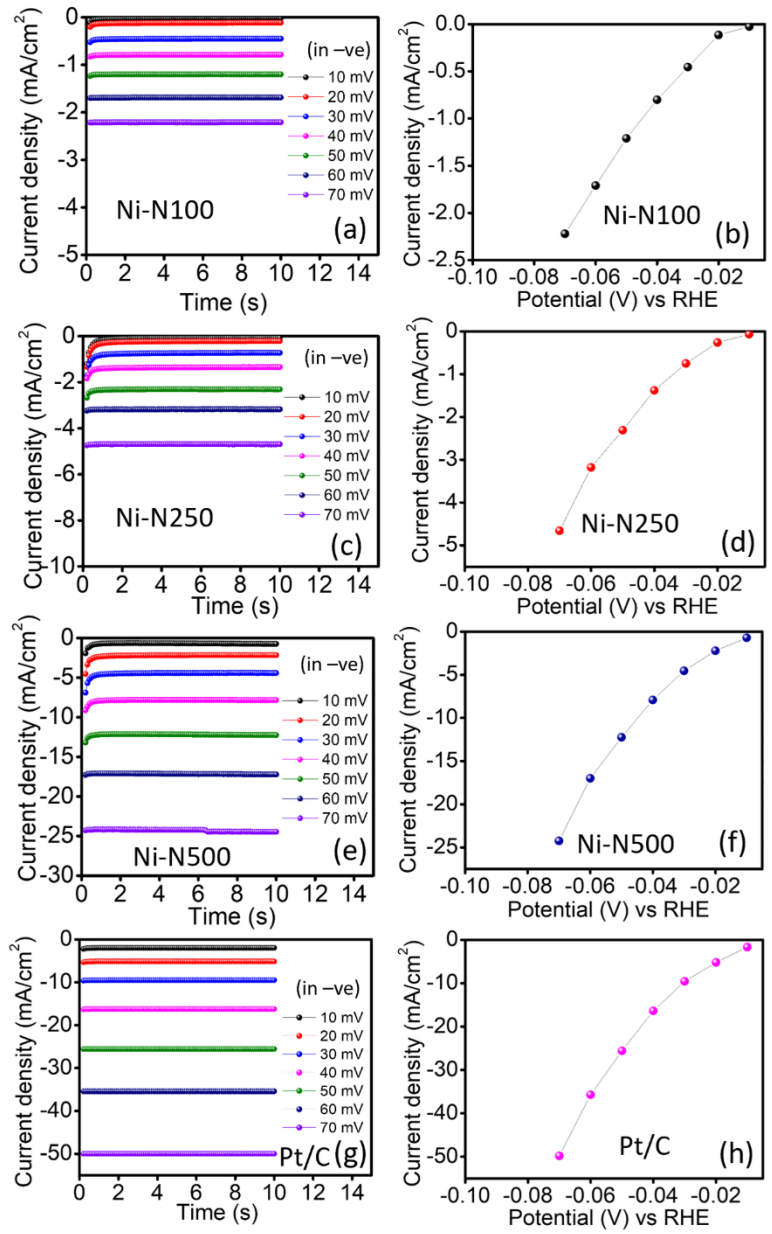

Fig. 13 (a), (c), (e), and (g) show the current vs. time plot, at applied potentials of -10, -20, -30, -40, -50, -60, and -70 mV for 10 seconds, for Ni-N100, Ni-N250, Ni-N500, and Pt/C samples, respectively. (b), (d), (f), and (h) show the plot for the observed current with respect to the applied potential for Ni-N100, Ni-N250, Ni-N500, and Pt/C samples, respectively.

The plot of potential versus current density is shown at 5 seconds.

Table-S6 Comparison of HER electrocatalytic activity of electrocatalyst in alkaline medium.

Electrocatalysts	Electrolyte	j@η	Reference
Ni-Sn@C NPs	1 M NaOH	4 $mAcm^{-2}$@1230 mV	[11]
N-C@Ni-Al_2O_3@GO	1 M NaOH	10 $mAcm^{-2}$@280 mV	[12]
Ni_3S_2/MWCNT-NC	1 M NaOH	10 $mAcm^{-2}$@480 mV	[13]
Ni-graphene	0.1 M KOH	10 $mAcm^{-2}$@300 mV	[14]
Ni-OCNT	1 M NaOH	10 $mAcm^{-2}$@222 mV	[15]
Co_2P/Ni_2P/CNT-3	1 M KOH	10 $mAcm^{-2}$@151 mV	[16]
Ni-$NCNT_{8.0}$	1 M KOH	10 $mAcm^{-2}$@147 mV	[17]
Ni-MoS_2/NCNTs-3	1 M KOH	10 $mAcm^{-2}$@179 mV	[18]
Ni-NC700	0.1 M KOH	10 $mAcm^{-2}$@301 mV	[19]
VC@NCNT	1 M KOH	10 $mAcm^{-2}$@159 mV	[20]
VN/Co@NCNT	1 M KOH	10 $mAcm^{-2}$@180 mV	[21]
Ni-Mo_2C@NPC	1 M KOH	10 $mAcm^{-2}$@183 mV	[22]
MoNiCNTs-3	1 M KOH	10 $mAcm^{-2}$@220 mV	[23]
Ni@NC_6-600	1 M KOH	10 $mAcm^{-2}$@181 mV	[24]
Ni-N500	**1M KOH**	**10 $mAcm^{-2}$@45.6 mV**	**This work**

S2.2.2 Activation energy

The temperature-dependent electron transport for HER kinetics was studied at the interface, and the corresponding activation energy (E_a) was estimated for each catalyst on Ni-NY (Y= 100, 250, and 500). Therefore, regarding this temperature dependence LSV polarization curves were recorded at 298, 303, 308, 313, and 318 K (**Fig**. S9**(**a), (c), and (e)). From the Arrhenius plot, slope $-E_a/R$ was estimated to extract the activation energy by plotting log *J* (mA cm^{-2}) against 1000/T at two different potentials (-0.075 and -0.100 V vs. RHE) (**Fig.** S9(b), (d), and (f))[6,25].

$$\ln(j) = \ln(A) - \frac{E_a}{R}\left(\frac{1}{T}\right)$$

where, *j* is the current density at -30 mV of HER for respective Ni-NY catalysts, A indicates the exponential factor, R denotes the Gas constant, and T exhibits the temperature (K).

slope (deducted from Figure S8 for different catalysts) = $\frac{E_a}{R}$

E_a = slope × R

= slope × (8.314 J mol^{-1})

(1 Joule = 6.242 ×10^{18} eV and 1 mol = 6.023 × 10^{23} molecules)

= slope × $\frac{8.314 \times 6.242 \times 10^{18}}{6.023 \times 10^{23}}$ eV/molecule

= slope × 8.61 ×10^{-5} eV/molecule

= slope × 0.0861 meV/molecule

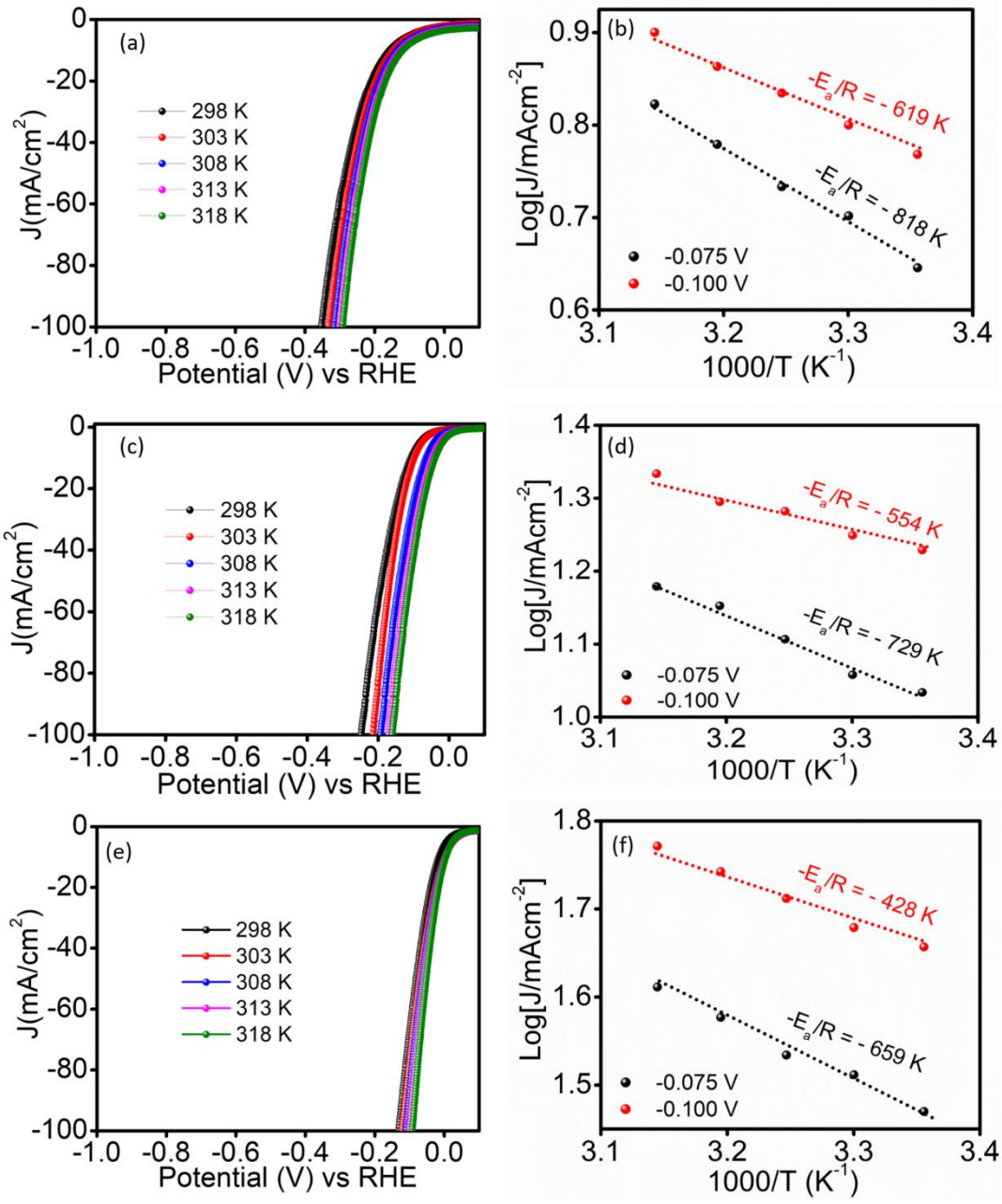

Fig. S14 (a), (c), and (e) show the HER-LSV polarization curve at temperature 298, 303, 308, 313, and 318K, and (b), (d), and (f) exhibits the Arrhenius plot to extract the activation energy at potentials -0.075 and -0.100 V vs. RHE respectively.

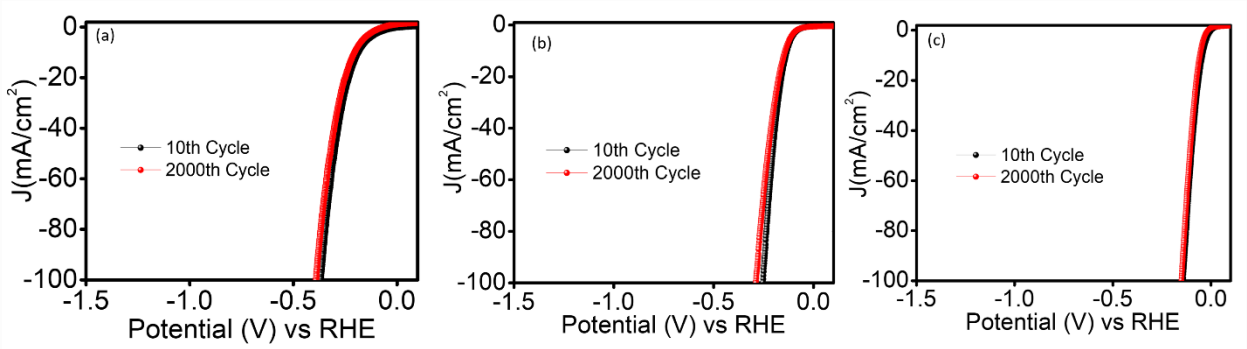

Fig. S15 (a), (b), and (c) show the LSV curves of Ni-N100, Ni-N250, and Ni-N500 electrocatalysts after the 10th and 2000th cycles of cyclic voltammogram.

S2.2.3 Impedance Analysis

The applied sinusoidal input voltage can be expressed as [26]-

$V_t = V_o \sin(\omega t)$ (S4)

For a purely capacitive circuit, the capacitor (C), the accumulated charges (q)at an applied voltage (V_t) can be related as,

$q = C\,V_t$

or, $q = C\,V_o \sin(\omega t)$ (S5)

and, $i = dq/dt = C\,(dV_t/dt)$

or, $i = \omega\,C\,V_o \cos(\omega t)$

or, $I = \frac{V_0}{X_C} \sin(\omega t + \frac{\pi}{2})$ (S6)

where X_C represents the capacitive reactance ($1/\omega C$) of the circuit.

The relationship between V_C and I, through a vector diagram (of a purely capacitive circuit), can be expressed as $V_C = -\,j\,X_C\,I$

In an RC circuit with the series connection of a resistance *R*, and a capacitance *C*, the voltage drop is a combination of voltage drop by the resistor and the capacitor; it can be expressed as:

$V = V_R + V_C$

or, $V = (R - j\,X_C)I$

or, $V = I\,Z$ (S7)

where $Z = R - j\,X_C$

or $Z = R - \frac{j}{\omega C}$, represents the impedance (Z).

Here the magnitude of *Z* can be written as:

$|Z|_{imp} = \sqrt{ZZ^*}$

or, $|Z|_{imp} = \sqrt{R^2 + X_C^2}$ (S8)

$|Z|_{imp} = \sqrt{R^2 + \frac{1}{(\omega C)^2}}$ (S9)

Keeping R constant, let's consider different conditions:

1) At a constant potential, if $|Z|_{imp}$ remains constant with an increase in frequency ω, it is clear that the value of capacitance (C) should decrease.
2) At a constant potential, if $|Z|_{imp}$ decreases with an increase in frequency, it suggests that the value of capacitance should decrease.
3) At a constant frequency, if $|Z|_{imp}$ decreases with an increase in potential, it suggests that the capacitance should increase.

We should keep in mind that a change in the value of the capacitance is directly related to the amount of charges stored in the capacitor.

S2.2.4 EIS at different applied potentials

(a) Comparing the $|Z|_{imp}$ in the LF region of the synthesized Ni-NY (Y=100, 250, and 500) electrocatalysts for any particular applied potential (**Fig**. 6 (b), (e), and (h)), it observed a sharp decrease of $|Z|_{imp}$ value as we move from Ni-N100 catalyst to Ni-N500 catalyst. This means that as the nitrogen content increases in the samples, the $|Z|_{imp}$ value decreases. This fact is associated with the creation of defective energy levels due to nitrogen dopants in carbon materials.

(b) Let's discuss how the capacitance decreases in our samples with the increase in frequency. At a certain applied (oscillatory) potential, as the frequency increases (in the very low-frequency region), the OH^- ions generated (due to the catalytic reaction, as discussed earlier) start to become more dynamic within the pores, which results in a diffusive motion that can be considered as leakage. This results in a decrease in capacitance. Hence, the capacitive reactance ($1/\omega C$) term remains almost constant. More accurately, this term slightly decreases with an increase in frequency (note the log scale!) due to a reduction in response (amplitude) of the ions to higher frequencies (low time availability to switch the direction of motion).

(c) Let's discuss the origin of the slight decrease of $|Z|_{imp}$ for the Ni-N100 catalyst compared to the other samples in the LF region. This aspect can be explained by using the previously discussed equation for $|Z|_{imp}$. The rate of decrease in $|Z|_{imp}$ with respect to frequency indicates that the resistance (R) and the capacitive reactance ($1/\omega C$), both should decrease. The resistance (R) is slightly higher for the Ni-N100 sample than the Ni-N500 sample, as can be referred to from **Fig**. 6((a), (d), and (g)). However, this small decrease in resistance cannot account for the faster decrease of $|Z|_{imp}$. Hence, the value of $1/\omega C$ needs to decrease faster over the observed frequency range to originate the more considerable decline in $|Z|_{imp}$. Here, as the increase in frequency is the same for all the samples under consideration, the reduction in the value of $1/\omega C$ is possible when capacitance increases at a slower rate, with the increase in frequency, for the Ni-N100 sample. This is evidenced by the sluggish fall in $|Z|_{imp}$ for the Ni-N100 in comparison to the other samples. In other words, the quick fall in $|Z|_{imp}$ for the Ni-N500 sample is a result of the sharp increase in capacitance across the narrow frequency range. The above-explained aspect could be a reason that the slope of the $|Z|_{imp}$ in the LF region decreases from higher to lower N-doped sample, i.e., from Ni-N500 sample to Ni-N100 sample (**Fig**. 6 (b, e, h)).

(d) Let's consider the theoretical work by Filipe et al. [27] on the charging dynamics inside arbitrary-sized cylindrical pores. Their study reveals that the charge stored per unit volume of the pore (volumetric capacitance) decreases with an increase in relative pore size. Furthermore, the volumetric capacitance decreases as the standard deviation of pore size increases for any average pore size. The standard deviation in pore size and pore volumes for Ni-NY samples are shown in **Fig**. S4. To verify the work of Filipe et al., it is important to consider the topological differences that we observed among our samples through their BET isotherms (**Fig**. 3(d)). The Ni-NY samples consist of non-uniform distribution of pores (sizes ranging between 1 nm and 13 nm) with an increase in pore volume from Ni-N100 to Ni-N500 sample. Clearly, the Ni-N100 sample consists of the highest amount of small-diameter pores among the samples (**Fig**. 3(d)). Here, although we apply a fixed potential, the tiny pores exhibit higher capacitance and behave as if a higher potential is being involved compared to the bigger pores. As the capacitance of the samples is related to the impedance through the eq-1, it is straightforward to prove that our work experimentally verifies all the details of the work by Filipe et al.

(e) As the frequency of the oscillating field increases from 10 mHz ($\log f \sim -2$) towards 1.3 Hz (i.e., $\log f \sim +0.12$, for the Ni-N100 sample), the phase lag of the generated ions gradually increases due to the electrostatic force and the steric hindrance in the pores of the sample. Through this process, the phase difference between the oscillating potential and the charged species generating the current starts increasing. A maximum phase difference of -77° (at $\log f = 0.12$) is observed for the applied potential of -30 mV. Note that the maximum phase difference did not reach 90°. This could be associated with the porous nature of our samples, where one may observe a distribution of electrostatic forces and steric hindrances. The pores, hills, and valleys on the surface of the graphitic carbon materials allow the diffusive motion of ions depending on the size of the pores.

(f) Let's consider the phase differences, where the amplitude of the potential gradually increases from -30 mV to -280 mV (see different curves in **Fig**. 6(c)). It is worth noting here that the ions are generated at the active sites (i.e., the C-atoms neighboring to the doped N) according to the reaction mechanism discussed earlier. It can be inferred that as the oscillating potential increases gradually, more ions (especially OH^- ions) are generated by the catalytic reaction. However, the

ion generation rate and their response vary as a response to the oscillating potential. For example, the generated ions in the pores start fluctuating with the oscillating potential. As the frequency increases, the fluctuating OH^- ions instantaneously sterically hinder the new charge from being created. Therefore, in this case, the phase difference starts increasing (from ~ 0° to ~ -90°) with the frequency.

(g) With further increase of frequency beyond 1.3 Hz (log f > 0.12), the phase lag slowly decreases (**Fig**. 6(c)) and approaches zero (~ 3° - 8°). This behavior is expected because, as the frequency increases logarithmically towards 10 kHz, the response of the ions gradually decreases (as the interaction time gradually decreases) with respect to the oscillating potential. The phase lag is controlled by the amount of pores and size in the sample. As explained earlier in the BET section, the highest pore volume is observed for the Ni-N250 sample (beyond a pore size of 9 nm), followed by the Ni-N500 and Ni-N100 samples. As the frequency is increased further (> log f = 4), the electrode material develops an opposite polarization oscillation, and the charged species completely stop responding to the oscillating field but respond to the opposite polarization of the electrode. Hence, the phase quickly drips to ~ - 180°.

(h) Let's compare the Bode phase plots, at a fixed frequency (and potential), obtained for different samples (**Fig**. 6(c), (f), and (i)). We observed a decrease in the phase at the same frequency and the same potential for the Ni-N100 to Ni-N500 samples. As we observe a larger pore volume (0.301 $cm^3\ g^{-1}$) for the Ni-N500 sample, the high surface area and higher defect amount (due to high N-doping) make the diffusion easier (i.e., low hindrance) as compared to that of the Ni-N100 and Ni-N250 samples (having pore volumes of 0.232 $cm^3\ g^{-1}$ and 0.293 $cm^3\ g^{-1}$, respectively). This is expected to be the major reason for exhibiting the minimal phase difference for all the frequencies (especially in the LF region) for the Ni-N500 sample, compared to that of the Ni-N100 and Ni-N250 samples. As the potential rises, the max phase angle changes rapidly from - 56° (for log f = -1.5) at -30 mV to ~ - 6° at -280 mV for the Ni-N500 sample. The higher pore volume, as well as a large amount of electrochemically active catalytic centers, makes diffusion easy through the carbon layer toward the metallic electrode surface. We expect that the diffusion process occurs only at the outer surface of N-doped layers. As we observed the smallest amount of high pore volume in the Ni-N100 sample, it shows the highest phase

difference of 7.6° at 10 kHz. Similarly, for the highest amount of large pores, the sample Ni-N250 shows the lowest phase difference (3.5°). Hence, the sequence of phase difference at 10 kHz is Ni-N100 (7.6°) > Ni-N500 (6°) > Ni-N250 (3.5°), as seen in **Fig**. 6 (c), (f), and (i).

S2.2.5 Discussion on the EIS behavior of the catalysts at a fixed potential

(a) The constant phase element CPE (Q_{dl}) was connected in parallel to charge transfer resistance (R_{ct}) at the electrode-electrolyte contact. To understand the rough nature of the electrode during the adsorption of charges, we added another constant phase element (Q_{ads}) and corresponding resistance (R_{ads}).

(b) According to eq-1, as the frequency of applied potential increases, the impedance $|Z|_{imp}$ needs to decrease monotonously (at the same rate for all three samples). However, the different rates of decrease, as observed for different samples, are associated with different capacitance of the samples. Hence, the varied capacitance of the samples is associated with the various sizes of the pores and their distribution. Here, the slight decrease in $|Z|_{imp}$ for the Ni-N100 sample can be associated with the higher volume of the smaller pores (and lower volume of bigger pores) (**Fig**. 3(d)) that increases capacitance (the capacity to store the charges statically (i.e., it doesn't easily allow the charges to flow easily)) as frequency increases. The ions move easily against steric hindrance in bigger pores; therefore, capacitance decreases sharply. This sharp decrease in capacitance harshly decreases the $|Z|_{imp}$ within a short frequency range. Comparing the above result of **Fig**. 7(c), it is obvious that in the LF region, the most defective graphitic carbon sample Ni-N500 allows easy diffusion of the ions; and, at the HF region, the ions have limited physical motion as a response to the applied frequency.

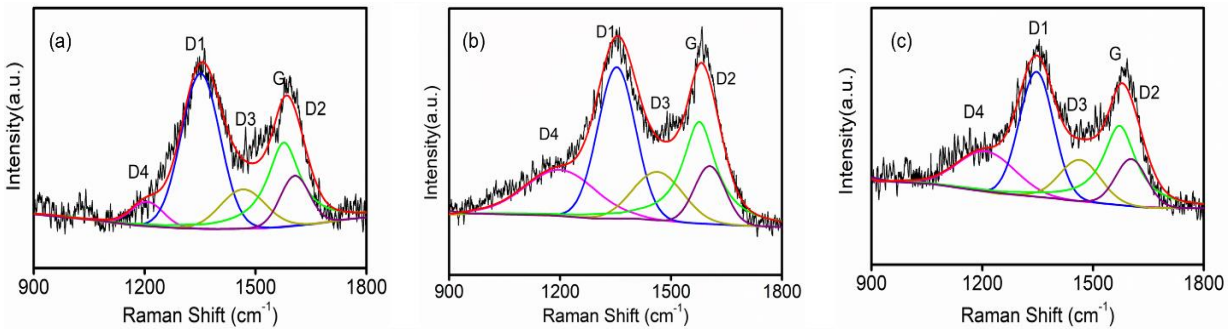

Fig. S16 (a), (b), and (c) show the Raman peak fitting for Ni-N100, Ni-N250, and Ni-N500, respectively, after HER measurement.

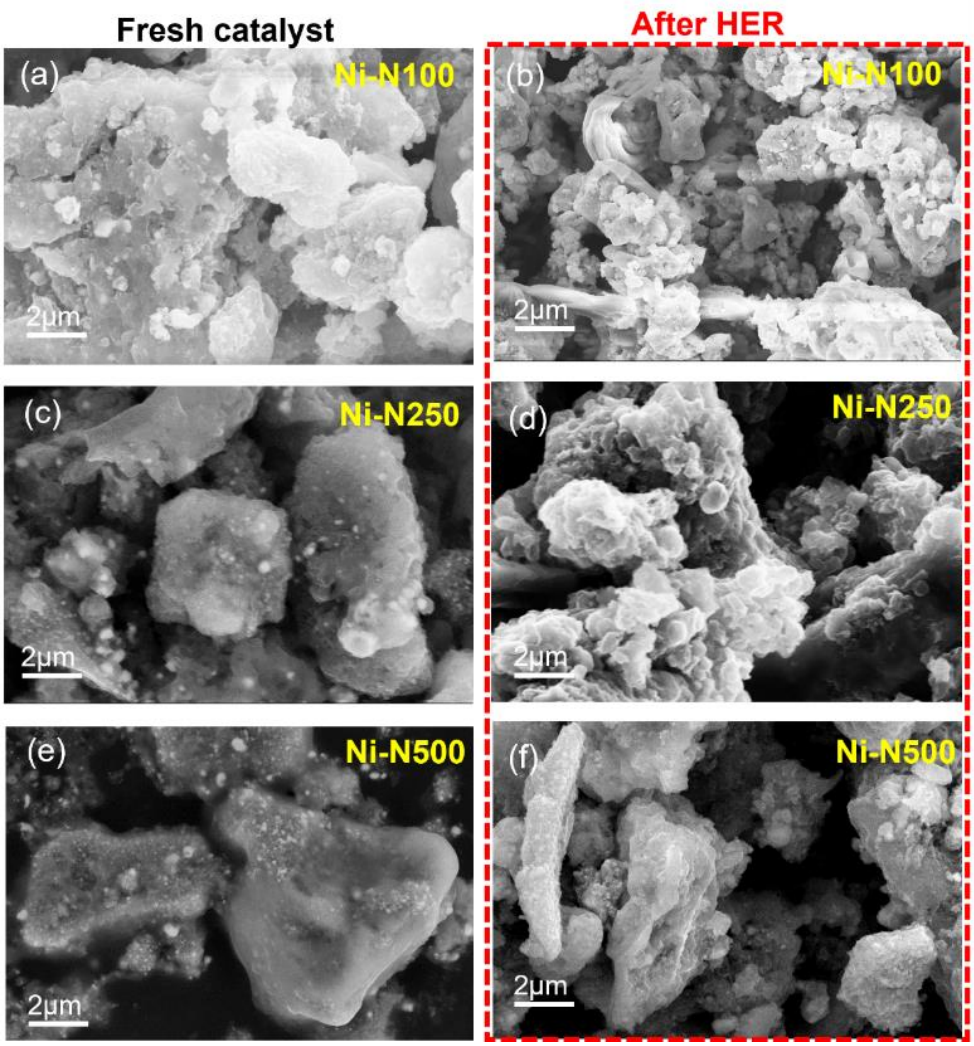

Fig. S17 (a), (c), and (e) SEM images of fresh catalysts and corresponding (b), (d), and (f) after HER catalysis for Ni-N100, Ni-N100, and Ni-N500, respectively.

References

(1) Nandan, R.; Gautam, A.; Nanda, K. K. Anthocephalus Cadamba Shaped FeNi Encapsulated Carbon Nanostructures for Metal-Air Batteries as a Resilient Bifunctional Oxygen Electrocatalyst. *J. Mater. Chem. A* **2018**, *6* (41), 20411–20420. https://doi.org/10.1039/c8ta05822a.

(2) Ramaswamy, N.; Tylus, U.; Jia, Q.; Mukerjee, S. Activity Descriptor Identification for Oxygen Reduction on Nonprecious Electrocatalysts: Linking Surface Science to Coordination Chemistry. *J. Am. Chem. Soc.* **2013**, *135* (41), 15443–15449. https://doi.org/10.1021/ja405149m.

(3) Kumar, R.; Kumar, A.; Verma, N.; Khopkar, V.; Philip, R.; Sahoo, B. Ni Nanoparticles Coated with Nitrogen-Doped Carbon for Optical Limiting Applications. *ACS Appl. Nano Mater.* **2020**, *3* (9), 8618–8631. https://doi.org/10.1021/acsanm.0c01284.

(4) Arkhipova, E. A.; Ivanov, A. S.; Strokova, N. E.; Chernyak, S. A.; Shumyantsev, A. V.; Maslakov, K. I.; Savilov, S. V.; Lunin, V. V. Structural Evolution of Nitrogen-Doped Carbon Nanotubes: From Synthesis and Oxidation to Thermal Defunctionalization. *Carbon N. Y.* **2017**, *125*, 20–31. https://doi.org/10.1016/j.carbon.2017.09.013.

(5) Nandan, R.; Gautam, A.; Tripathi, S.; Nanda, K. K. A Comprehensive Analysis and Rational Designing of Efficient Fe-Based Oxygen Electrocatalysts for Metal-Air Batteries. *J. Mater. Chem. A* **2018**, *6* (18), 8537–8548. https://doi.org/10.1039/c8ta01938j.

(6) Nandan, R.; Devi, H. R.; Kumar, R.; Singh, A. K.; Srivastava, C.; Nanda, K. K. Inner Sphere Electron Transfer Promotion on Homogeneously Dispersed Fe-N_XCenters for Energy-Efficient Oxygen Reduction Reaction. *ACS Appl. Mater. Interfaces* **2020**, *12* (32), 36026–36039. https://doi.org/10.1021/acsami.0c08086.

(7) Yadav, A.; Kumar, R.; Pandey, U. P.; Sahoo, B. Role of Oxygen Functionalities of GO in Corrosion Protection of Metallic Fe. *Carbon N. Y.* **2021**, *173*, 350–363. https://doi.org/10.1016/j.carbon.2020.11.029.

(8) Preda, I.; Gutiérrez, A.; Abbate, M.; Yubero, F.; Méndez, J.; Alvarez, L.; Soriano, L. Interface Effects in the Ni 2p X-Ray Photoelectron Spectra of NiO Thin Films Grown on

Oxide Substrates. *Phys. Rev. B - Condens. Matter Mater. Phys.* **2008**, *77* (7), 1–7. https://doi.org/10.1103/PhysRevB.77.075411.

(9) Kuang, M.; Wang, Q.; Han, P.; Zheng, G. Cu, Co-Embedded N-Enriched Mesoporous Carbon for Efficient Oxygen Reduction and Hydrogen Evolution Reactions. *Adv. Energy Mater.* **2017**, *7* (17), 1–8. https://doi.org/10.1002/aenm.201700193.

(10) Devi, H. R.; Nandan, R.; Nanda, K. K. Mechanistic Investigation into Efficient Water Oxidation by Co-Ni-Based Hybrid Oxide-Hydroxide Flowers. *ACS Appl. Mater. Interfaces* **2020**, *12* (12), 13888–13895. https://doi.org/10.1021/acsami.9b22956.

(11) Lang, L.; Shi, Y.; Wang, J.; Wang, F. Bin; Xia, X. H. Hollow Core-Shell Structured Ni-Sn@C Nanoparticles: A Novel Electrocatalyst for the Hydrogen Evolution Reaction. *ACS Appl. Mater. Interfaces* **2015**, *7* (17), 9098–9102. https://doi.org/10.1021/acsami.5b00873.

(12) Wang, J.; Qiu, T.; Chen, X.; Lu, Y.; Yang, W. N-Doped Carbon@Ni-Al_2O_3 Nanosheet Array@graphene Oxide Composite as an Electrocatalyst for Hydrogen Evolution Reaction in Alkaline Medium. *J. Power Sources* **2015**, *293*, 178–186. https://doi.org/10.1016/j.jpowsour.2015.05.080.

(13) Lin, T. W.; Liu, C. J.; Dai, C. S. Ni_3S_2/Carbon Nanotube Nanocomposite as Electrode Material for Hydrogen Evolution Reaction in Alkaline Electrolyte and Enzyme-Free Glucose Detection. *Appl. Catal. B Environ.* **2014**, *154–155*, 213–220. https://doi.org/10.1016/j.apcatb.2014.02.017.

(14) Huang, Y. guo; Fan, H. lin; Chen, Z. kai; Gu, C. bing; Sun, M. xue; Wang, H. qiang; Li, Q. yu. The Effect of Graphene for the Hydrogen Evolution Reaction in Alkaline Medium. *Int. J. Hydrogen Energy* **2016**, *41* (6), 3786–3793. https://doi.org/10.1016/j.ijhydene.2015.12.113.

(15) Wang, L.; Li, Y.; Yin, X.; Wang, Y.; Lu, L.; Song, A.; Xia, M.; Li, Z.; Qin, X.; Shao, G. Comparison of Three Nickel-Based Carbon Composite Catalysts for Hydrogen Evolution Reaction in Alkaline Solution. *Int. J. Hydrogen Energy* **2017**, *42* (36), 22655–22662. https://doi.org/10.1016/j.ijhydene.2017.06.215.

(16) Ding, Z.; Yu, H.; Liu, X.; He, N.; Chen, X.; Li, H.; Wang, M.; Yamauchi, Y.; Xu, X.;

Amin, M. A.; Lu, T.; Pan, L. Prussian Blue Analogue Derived Cobalt–Nickel Phosphide/Carbon Nanotube Composite as Electrocatalyst for Efficient and Stable Hydrogen Evolution Reaction in Wide-PH Environment. *J. Colloid Interface Sci.* **2022**, *616*, 210–220. https://doi.org/10.1016/j.jcis.2022.02.039.

(17) Oluigbo, C. J.; Xu, Y.; Louis, H.; Yusuf, A. B.; Yaseen, W.; Ullah, N.; Alagarasan, K. J.; Xie, M.; Ekpenyong, E. E.; Xie, J. Controllable Fabrication of Abundant Nickel-Nitrogen Doped CNT Electrocatalyst for Robust Hydrogen Evolution Reaction. *Appl. Surf. Sci.* **2021**, *562* (April), 150161. https://doi.org/10.1016/j.apsusc.2021.150161.

(18) Dong, T.; Zhang, X.; Wang, P.; Chen, H. S.; Yang, P. Formation of Ni-Doped MoS2 Nanosheets on N-Doped Carbon Nanotubes towards Superior Hydrogen Evolution. *Electrochim. Acta* **2020**, *338*, 135885. https://doi.org/10.1016/j.electacta.2020.135885.

(19) Devi, B.; Koner, R. R.; Halder, A. Ni(II)-Dimeric Complex-Derived Nitrogen-Doped Graphitized Carbon-Encapsulated Nickel Nanoparticles: Efficient Trifunctional Electrocatalyst for Oxygen Reduction Reaction, Oxygen Evolution Reaction, and Hydrogen Evolution Reaction. *ACS Sustain. Chem. Eng.* **2019**, *7* (2), 2187–2199. https://doi.org/10.1021/acssuschemeng.8b04883.

(20) Cao, L.; Zhang, N.; Feng, L.; Huang, J.; Feng, Y.; Li, W.; Yang, D.; Liu, Q. Well-Dispersed Ultrasmall VC Nanoparticles Embedded in N-Doped Carbon Nanotubes as Highly Efficient Electrocatalysts for Hydrogen Evolution Reaction. *Nanoscale* **2018**, *10* (29), 14272–14279. https://doi.org/10.1039/c8nr03930e.

(21) Feng, L.; Feng, L.; Huang, J.; Cao, L.; Kajiyoshi, K. Ultrafine VN Nanoparticles Confined in Co@N-Doped Carbon Nanotubes for Boosted Hydrogen Evolution Reaction. *J. Alloys Compd.* **2021**, *853*. https://doi.org/10.1016/j.jallcom.2020.157257.

(22) Lu, Y.; Yue, C.; Li, Y.; Bao, W.; Guo, X.; Yang, W.; Liu, Z.; Jiang, P.; Yan, W.; Liu, S.; Pan, Y.; Liu, Y. Atomically Dispersed Ni on Mo_2C Embedded in N, P Co-Doped Carbon Derived from Polyoxometalate Supramolecule for High-Efficiency Hydrogen Evolution Electrocatalysis. *Appl. Catal. B Environ.* **2021**, *296* (April), 120336. https://doi.org/10.1016/j.apcatb.2021.120336.

(23) Zhang, X.; Yang, P.; Jiang, S. P. Ni Diffusion in Vertical Growth of MoS_2 Nanosheets on Carbon Nanotubes towards Highly Efficient Hydrogen Evolution. *Carbon N. Y.* **2021**, *175*, 176–186. https://doi.org/10.1016/j.carbon.2021.01.010.

(24) Cheng, N.; Wang, N.; Ren, L.; Casillas-Garcia, G.; Liu, N.; Liu, Y.; Xu, X.; Hao, W.; Dou, S. X.; Du, Y. In-Situ Grafting of N-Doped Carbon Nanotubes with Ni Encapsulation onto MOF-Derived Hierarchical Hybrids for Efficient Electrocatalytic Hydrogen Evolution. *Carbon N. Y.* **2020**, *163*, 178–185. https://doi.org/10.1016/j.carbon.2020.03.017.

(25) Santra, S.; Das, D.; Das, N. S.; Nanda, K. K. An Efficient On-Board Metal-Free Nanocatalyst for Controlled Room Temperature Hydrogen Production. *Chem. Sci.* **2017**, *8* (4), 2994–3001. https://doi.org/10.1039/C7SC00162B.

(26) Allen J. Bard, L. R. F. *Electrochemical Methods Fundamentals and Applications*, Second edi.; Swain, E., Ed.; JOHN WILEY & SONS, INC: Texas, Austin, 1980.

(27) Henrique, F.; Zuk, P. J.; Gupta, A. Charging Dynamics of Electrical Double Layers inside a Cylindrical Pore: Predicting the Effects of Arbitrary Pore Size. *Soft Matter* **2022**, *18* (1), 198–213. https://doi.org/10.1039/d1sm01239h.